High-dimensional Steady-state Security Region Boundary Approximation in Power Systems Using Feature Non-linear Converter and Improved Oblique Decision Tree

Yuxin Dai, Jun Zhang, Peidong Xu, Tianlu Gao, and David Wenzhong Gao

Abstract—The steady-state security region (SSR) offers robust support for the security assessment and control of new power systems with high uncertainty and fluctuation. However, accurately solving the steady-state security region boundary (SS-RB), which is high-dimensional, non-convex, and non-linear, presents a significant challenge. To address this problem, this paper proposes a method for approximating the SSRB in power systems using the feature non-linear converter and improved oblique decision tree. First, to better characterize the SSRB, boundary samples are generated using the proposed sampling method. These samples are distributed within a limited distance near the SSRB. Then, to handle the high-dimensionality, nonconvexity and non-linearity of the SSRB, boundary samples are converted from the original power injection space to a new feature space using the designed feature non-linear converter. Consequently, in this feature space, boundary samples are linearly separated using the proposed information gain rate based weighted oblique decision tree. Finally, the effectiveness and generality of the proposed sampling method are verified on the WECC 3-machine 9-bus system and IEEE 118-bus system.

Index Terms—Steady-state security region, boundary sample generation, feature non-linear conversion, oblique decision tree.

I. INTRODUCTION

WITH the significant increase in the proportion of renewable energy and power electronic equipment integrated into the power system, the uncertainty and fluctuation of the system have risen dramatically, and the operating mode has become more variable [1]-[3]. As a result, the traditional pointwise method may no longer be applicable due

Manuscript received: February 21, 2024; revised: April 8, 2024; accepted: April 29, 2024. Date of CrossCheck: April 29, 2024. Date of online publication: August 1, 2024.

DOI: 10.35833/MPCE.2024.000188

to its high computational demands and low efficiency [4], [5].

The steady-state security region (SSR), as the set of all operating points on the power injection space that satisfy the power flow equation and system security constraints, can provide powerful support for the security assessment and control of power systems with high uncertainty and fluctuation [6]-[8]. Depending on the security constraints involved, SSR can be further divided into thermal stability security region, static voltage security region, and other categories, each suitable for specific applications [9]. However, due to the non-linearity of the power flow equation and diverse security constraints, the steady-state security region boundary (SSRB) is non-convex and non-linear. Accurately obtaining the SSRB has become a bottleneck in its application [4].

The theoretical derivation of the SSR is achieved by combining the decoupled power flow equation with the Leray-Schauder fixed point [10]. In [11], a scalable optimization framework based on Brouwer's fixed point is proposed to estimate the convex inner approximation of the SSR. Additionally, [12] constructs convex constraints on algebraic sets defined by equality and inequality constraints and applies them to power flow feasibility.

The methods mentioned above theoretically derive the SSR from the power flow equation and its security constraints. However, these methods are often conservative and may fail to include some secure operating points that are of interest to operators. Therefore, there is a need to develop SSR solutions with higher accuracy. In [4], SSR is proven to be uniquely determined, connected, independent of the operating state, and internally void-free under a given network topology and system component parameters.

Based on the above conclusions, some research works attempt to address the SSRB from a data-driven perspective. In [13]-[15], the methods for searching critical points and then utilizing segmented linear approximation to fit the boundaries are proposed. Additionally, a bootstrap-based method is proposed for coefficient approximation of the hyperplane of the thermal security region boundary [16]. In [17], a fast method for generating hyperplane expressions for SSR is proposed and applied to voltage control. All of the



This work was supported by the National Key Research and Development Program of China (No. 2018AAA0101504) and the Science and Technology Project of State Grid Corporation of China "fundamental theory of human inthe-loop hybrid-augmented intelligence for power grid dispatch and control".

This article is distributed under the terms of the Creative Commons Attribution 4.0 International License (http://creativecommons.org/licenses/by/4.0/).

Y. Dai, J. Zhang (corresponding author), P. Xu, and T. Gao are with the School of Electrical Engineering and Automation, Wuhan University, Wuhan 430072, China (e-mail: YuxinDai@whu.edu.cn; jun. zhang. ee@whu.edu.cn; xupd@whu.edu.cn; tianlu.gao@whu.edu.cn).

D. W. Gao is with Department of Electrical and Computer Engineering, Denver, USA (e-mail: wenzhong.2001.gao@ieee.org).

above methods provide boundary expressions by fitting hyperplane coefficients. Another idea is to model the boundary solving problem as a classification problem, thus indirectly approximating its boundary. Based on this idea, [18] presents a data-driven method for transient stability assessment. In [19], a convolutional neural network (CNN) based transient stability assessment and margin prediction method is proposed. In other fields, [20] defines the SSR of multi-energy systems and provides a solving method. A method for constructing SSR in distribution systems with high penetration of distributed energy resources is also proposed [21].

Nevertheless, accurately solving the SSRB remains challenging. This is due to the non-linearity of the power flow equation in AC systems and the numerous complex security constraints, making SSRB non-convex and non-linear. With the increasing size of power systems and the growing number of power electronic devices connected to the grid, these problems are further aggravated. As a result, the aforementioned methods often suffer from significant errors. Meanwhile, the methods proposed above are challenging to be applied to solve high-dimensional SSRB.

In recent years, deep neural networks (DNNs) [22] have been widely utilized in various areas of power systems such as transient stability assessment [23], [24], fault diagnosis [25]-[28] and load forecasting [29]-[31] due to their powerful ability to extract non-linear features. Consequently, we anticipate that DNNs will also be effective in capturing the non-linear relationships between variables and boundaries in the high-dimensional power injection space. However, this poses new challenges as DNNs are end-to-end models which cannot present the learned boundary information to humans. Besides, decision trees (DTs) and their derivative algorithms have gained significance in the field of power system security assessment [32], [33], as they offer an inherent model mechanism that can be easily converted into boundary expressions for subsequent security assessment and control. However, DTs are essentially linear classification models and may not perform satisfactorily on non-linearly separable datasets, thereby limiting their application scope.

Based on the analysis presented above, combined with the SSR property proven by [4], this paper proposes a high-dimensional SSRB approximation method using the feature non-linear converter and improved oblique DT. The contributions of this paper can be summarized as follows.

- 1) For the high-dimensional, non-convex, and non-linear SSRB, a novel SSRB approximation framework via the feature non-linear converter and information gain rate based weighted oblique DT (IGR-WODT) is proposed.
- 2) An improved sampling method is proposed to search for boundary sample pairs which are distributed near the SS-RB in order to facilitate the subsequent model to better learn the characteristics of SSRB.
- 3) The DNN-based model is designed to address the non-linearly separable issue within the dataset, and IGR-WODT is employed to approximate SSRB.
- 4) The proposed sampling method successfully approximates the high-dimensional SSRB and reduces the error between the approximated boundary and the actual one, which

are verified on the WECC 3-machine 9-bus system and IEEE 118-bus system.

The remainder of this paper is organized as follows. Section II first introduces the SSR model of power systems. Section III details high-dimensional SSRB approximation. Section IV presents the case study. Finally, Section V summarizes the paper.

II. SSR MODEL OF POWER SYSTEMS

The SSR model of power systems is defined as the set of points satisfying the power flow equation and operating security constraints [10]. It can be expressed as:

$$\begin{cases}
\mathbb{R}_{ss} = \mathbb{R}_{U} \cap \mathbb{R}_{P} \cap \mathbb{R}_{Q} \cap \mathbb{R}_{P_{b}} \\
\mathbb{R}_{U} = \begin{cases}
\mathbf{x} \middle| \phi(\mathbf{x}, \mathbf{y}) = 0 \\
U_{i}^{\min} \leq U_{i} \leq U_{i}^{\max} \quad \forall i \in N
\end{cases} \\
\mathbb{R}_{P} = \begin{cases}
\mathbf{x} \middle| \phi(\mathbf{x}, \mathbf{y}) = 0 \\
P_{g, \min, i} \leq P_{g, i} \leq P_{g, \max, i} \quad \forall i \in N_{g}
\end{cases} \\
\mathbb{R}_{Q} = \begin{cases}
\mathbf{x} \middle| \phi(\mathbf{x}, \mathbf{y}) = 0 \\
Q_{g, \min, i} \leq Q_{g, i} \leq Q_{g, \max, i} \quad \forall i \in N_{g}
\end{cases} \\
\mathbb{R}_{P_{b}} = \begin{cases}
\mathbf{x} \middle| \phi(\mathbf{x}, \mathbf{y}) = 0 \\
-P_{b, i-j}^{\max} \leq P_{b, i-j} \leq P_{b, i-j}^{\max} \quad \forall i, j \in N
\end{cases}$$

where \mathbb{R}_U is the static voltage security region satisfying the voltage constraints; \mathbb{R}_P is the static generator active output security region satisfying the generator active output constraints; \mathbb{R}_{O} is the static generator reactive output security region satisfying the generator reactive output constraints; \mathbb{R}_{p} is the branch thermal stability security region satisfying the system branch transmission power constraints; \mathbb{R}_{ss} is the whole SSR, which shows the intersection of \mathbb{R}_U , \mathbb{R}_P , \mathbb{R}_Q , and \mathbb{R}_{p} ; y is the state variable vector; x is the power injection vector; $\phi(x,y)=0$ is the AC power flow equation in power systems; N is the set of system buses; N_{σ} is the set of system generators; U_i^{\min} and U_i^{\max} are the lower and upper voltage limits of the i^{th} bus, respectively; $P_{g,\min,i}$ and $P_{g,\max,i}$ are the lower and upper limits of active output of the i^{th} generator, respectively; $Q_{g,\min,i}$ and $Q_{g,\max,i}$ are the lower and upper limits of reactive output of the i^{th} generator, respectively; and $P_{b,i-j}^{\max}$ and $-P_{b,i-j}^{\max}$ are the forward and reverse transmission power limits of the branch connected buses i and j, re-

In the case of approximating local balance of reactive power, only the SSR under active power injection needs to be considered.

$$\begin{cases}
\mathbb{R}_{ss} = \left\{ \mathbf{x}_{P} | \mathbf{x} \in \mathbb{R}_{U} \cap \mathbb{R}_{P} \cap \mathbb{R}_{Q} \cap \mathbb{R}_{P_{b}} \right\} \\
\mathbf{x}_{P} = \left[P_{g,i}, P_{l,j} \right] \quad \forall i \in N_{g}, \forall j \in N
\end{cases}$$
(2)

where $\mathbf{x} = \begin{bmatrix} \mathbf{x}_P, \mathbf{x}_Q \end{bmatrix}$; \mathbf{x}_P is the active power injection at each bus; $\mathbf{x}_Q = \mathbf{c}$ is the reactive power injection at each bus and \mathbf{c} denotes a constant vector; $P_{g,i}$ is the active power output of the i^{th} generator; and $P_{l,j}$ is the load value of the j^{th} bus.

The SSR in the active power injection space is studied as the set of operating points at which various security constraints are satisfied by the system unit combinations and load demands under a specific reactive power configuration.

As proven in [4], the SSR is uniquely determined, connected, and independent of the operating state, and it is internally void-free under a given network topology and system component parameters. Consequently, if an operating point in the active power injection space is situated within the SSR and it slowly changes its active power injection in a quasi-steady state form along either direction, it will eventually reach the security region boundaries. The region enclosed by these boundaries constitutes the SSR. Therefore, it is feasible to initiate from certain points within the SSR and find sufficient boundary points to approximate the boundary.

III. HIGH-DIMENSIONAL SSRB APPROXIMATION

In large-scale power systems, SSRB is high-dimensional,

non-convex, and non-linear,

As illustrated in Fig. 1, this paper models the boundary solving problem as a binary classification problem. If the classification model can accurately distinguish between secure and insecure samples, it can be regarded as an approximation of the actual boundary. Subsequently, the proposed IGR-WODT is transformed into the form of boundary hyperplanes to accomplish boundary approximation. In Fig. 1, $Conv1D(\cdot)$ represents a CNN layer; x is the input data; w_1 is the weight parameters of CNN; x_1 is the output of CNN layer; x_{i-1} and x_i are the outputs of the $(i-1)^{th}$ and i^{th} layers, respectively; N_S is the number of secure samples within N_{init} samples; $relu(\cdot)$ and $softmax(\cdot)$ are the activation functions of neural network; z is the vector in the feature space; and y is the output of the whole neural network.

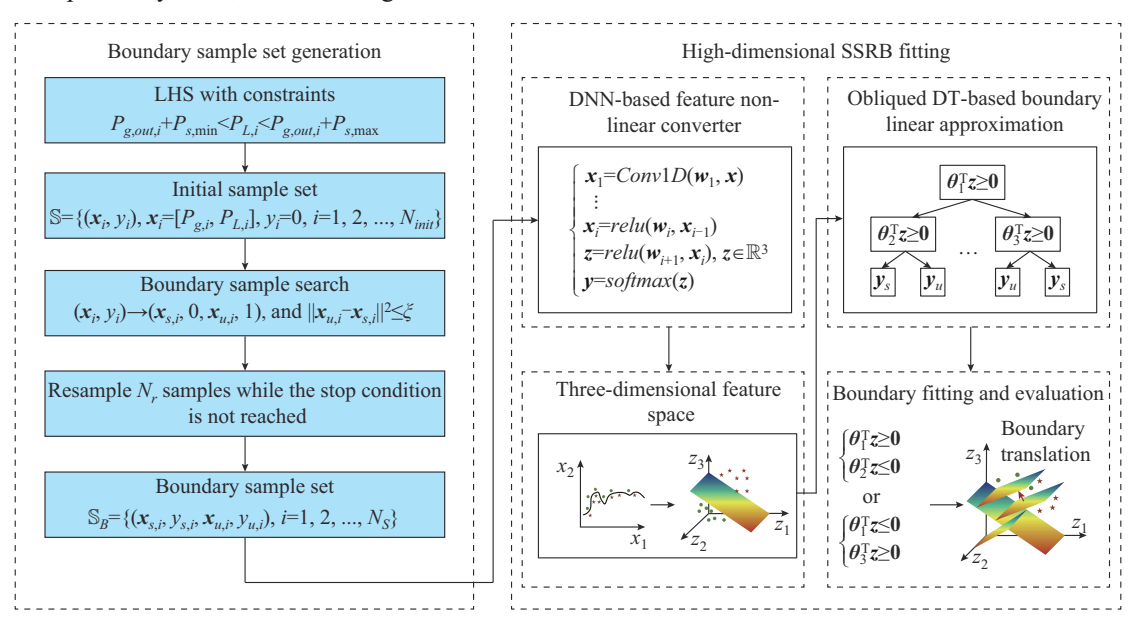


Fig. 1. Framework of high-dimensional SSRB approximation.

The whole work consists of two parts. (1) Boundary sample set generation: the aim of this part is to search for a large number of boundary sample sets that are distributed near the SSRB, thereby providing a suitable dataset for the training and testing of the subsequent classification model. To address the issue of unbalanced samples and uncontrolled distances of samples from the boundary in traditional sampling methods, firstly, the generator output and load values are sampled using the improved Latin hypercube sampling (LHS) algorithm to form the initial sample set. Then, the boundary sample search is performed, and a resampling mechanism that considers sampling gaps is proposed to ultimately form the boundary sample set. 2 High-dimensional SSRB approximation: this part is based on the generated boundary sample set, training a classification model, and then converting the model into the form of boundary hyperplanes. Given the non-linear separability of the boundary sample set in high-dimensional SSR, firstly, the original power injection space is converted into the feature space by the feature non-linear conversion using DNNs. The samples in

the feature space are approximately linearly separable. Secondly, in the feature space, the security region boundary is linearly fitted based on the proposed IGR-WODT. Then, the SSRB is obtained by the trained IGR-WODT and conservatively translated to ensure the security of the boundary. Finally, the fitted SSRB is evaluated and verified on a large number of randomly generated operating points.

A. Boundary Sample Set Generation for SSR

1) Initial Sample Set Generation

In the initial sample set generation process, the generator output is first sampled based on the LHS algorithm. Specifically, we set an N nodal power system containing N_l load nodes and N_g generators. The lower and upper limits of the j^{th} generator output are shown in (3).

$$P_{g, \min, j}, P_{g, \max, j} = 1, 2, ..., N_g$$
 (3)

We first define the sampling number of initial sample set as N_{init} , and then, we sample the generator output data based on the LHS, as denoted in (4).

$$\mathbf{P}_{g} = \begin{bmatrix} P_{g,1,1} & P_{g,1,2} & \cdots & P_{g,1,N_{g}} \\ P_{g,2,1} & P_{g,2,2} & \cdots & P_{g,2,N_{g}} \\ \vdots & & & \vdots \\ P_{g,N_{inii},1} & P_{g,N_{inii},2} & \cdots & P_{g,N_{inii},N_{g}} \end{bmatrix}$$
(4)

where $P_{g,i,j}$ is the j^{th} generator output in the i^{th} sample.

$$P_{g,\min,j} \le P_{g,i,j} \le P_{g,\max,j} \quad \forall i,j \tag{5}$$

In this paper, samples located within the security region are defined as secure samples and labeled as 0. Conversely, samples outside the security region are defined as insecure samples and labeled as 1. As the proposed sampling method in this paper requires searching for boundary samples based on a significant number of secure samples, it is essential to increase the proportion of secure samples among N_{init} samples. To this end, this part proposes a method for sampling load values that considers the constraints of the generator output. Specifically, for the ith sample, the total generator output is $P_{g,out,i} = \sum_{i=1}^{s} P_{g,i,j}$, and the upper and lower limits of the generator output at the slacking bus are set as $P_{\rm s,min}$ and $P_{s,\text{max}}$, respectively. The total sampling value of N_l load nodes is set to be $P_{L,i} = \sum_{i=1}^{N_i} P_{L,i,j}$, where the $P_{L,i,j}$ is the load value of j^{th} load bus in the i^{th} sample. To meet the output constraints of the generator at the slacking bus without considering the network loss, it is necessary for $P_{L,i}$ to satis-

$$P_{g,out,i} + P_{s,\min} \le P_{L,i} \le P_{g,out,i} + P_{s,\max} \quad \forall P_{l,i,j} \ge 0, j = 1, 2, ..., N_l$$
(6)

The constraints in (6) enclose a convex hyper-polyhedron in the N_{Γ} -dimensional space. To achieve uniform sampling of load values inside the hyper-polyhedron as above, the problem is modeled as sampling the N_{Γ} -dimensional vectors in the hyper-polyhedron, as shown in (7).

$$AP_{l} \leq b \tag{7}$$

where $\mathbf{A} \in \mathbb{R}^{(N_l+2) \times N_l}$ is the hyperplane normal vector; $\mathbf{P}_l \in \mathbb{R}^{N_l \times 1}$ represent the variables to be solved; and $\mathbf{b} \in \mathbb{R}^{(N_l+2) \times 1}$ is a constant vector.

Step 1: construct the linear objective function as:

$$\begin{cases} f\left(\boldsymbol{P}_{l}\right) = \min \sum_{i=1}^{N_{l}} P_{l,i} \\ \text{s.t. } A\boldsymbol{P}_{l} \leq \boldsymbol{b} \end{cases}$$
 (8)

The optimal solution $P_{l,0}$, which is the initial value of P_l , is obtained using the linear programming method. $P_{l,0}$ is a vertex of the hyper-polyhedron represented by (7), as shown in Fig. 1.

Step 2: solve the center of the hyper-polyhedron with $P_{l,0}$. For this purpose, we construct a non-linear optimization problem.

$$\begin{cases} \boldsymbol{P}_{l,cen} = \min \prod_{i=1}^{N_l+2} \left(\boldsymbol{A}_{i,:} \boldsymbol{P}_l - \boldsymbol{b}_i \right) \\ \text{s.t. } \boldsymbol{A} \boldsymbol{P}_l \le \boldsymbol{b} \end{cases}$$
(9)

where A_i is the i^{th} row vector of matrix A; and b_i is the i^{th}

feature of b.

Step 3: as shown in Fig. 1, we randomly initialize a sampling direction $\mathbf{u} \in \mathbb{R}^{N_t \times 1}$. Let the line passing through the center point $\mathbf{P}_{l,cen}$ with a line direction vector $\mathbf{u} \in \mathbb{R}^{N_t \times 1}$ be denoted as $\mathbf{r}(t) = \mathbf{P}_{l,cen} + t\mathbf{u}$, $\mathbf{u} \notin \mathbf{A}$. Then, we solve for the intersection points between the line $\mathbf{r}(t)$ and the convex polytope $\mathbf{A}\mathbf{x} = \mathbf{b}$, i.e.:

$$O = P_{l,cen} + \frac{b - AP_{l,cen}}{Au} u \tag{10}$$

where O represents the intersection point of the line r(t) and the N_l+2 hyperplanes represented by Ax=b. In fact, among those N_l+2 intersection points, only two are on the convex polytope, denoted as O_1 and O_2 .

$$\begin{cases} w = \frac{b - AP_{l,cen}}{Au} \\ w_p = w[Au > 0] \\ w_n = w[Au < 0] \end{cases}$$
(11)

where Au represents the projection of the line direction vector u onto A; and w[Au>0] and w[Au<0] represent that the values of w correspond to the indices in Au where the features are less than and greater than 0, respectively. The positive or negative value of Au indicates whether the intersection points are located in the direction of u or -u with respect to $P_{l,cen}$, respectively, as shown in Fig. 1. Thus, the points O_1 and O_2 can be calculated as:

$$\begin{cases}
\mathbf{o}_{1} = \max(\mathbf{w}_{n}) \\
\mathbf{o}_{2} = \min(\mathbf{w}_{p}) \\
\mathbf{O}_{1} = \mathbf{P}_{l,cen} + \mathbf{o}_{1}\mathbf{u} \\
\mathbf{O}_{2} = \mathbf{P}_{l,cen} + \mathbf{o}_{2}\mathbf{u}
\end{cases}$$
(12)

Step 4: make uniform sampling among the points O_1 and O_2 , as shown in Fig. 2, i.e., randomly generate $\mu \in [0, 1]$, to obtain the sampling points as:

$$\boldsymbol{P}_{l,sam} = \boldsymbol{P}_{l,cen} + \left(\boldsymbol{o}_1 + \mu \left(\boldsymbol{o}_2 - \boldsymbol{o}_1\right)\right) \boldsymbol{u}$$
 (13)

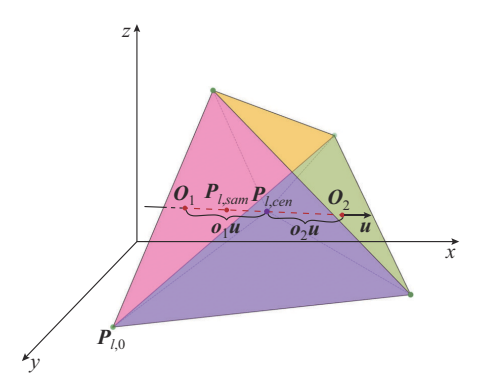


Fig. 2. Sampling process of initial samples.

Following *Steps 1-4*, the load values in N_{init} samples are obtained. The secure samples within N_{init} samples are selected and formed into the initial sample set, $S = (9) \quad (x_i, 0), i \in 1, 2, ..., N_S$, where $x_i = [P_{g,i}, P_{L,i}]$, and $P_{g,i}$ is the generator output vector of the i^{th} sample, and $P_{L,i}$ is the load value vector of the i^{th} sample.

2) Boundary Sample Search

As shown in Fig. 3, the problem of SSRB solution is modeled as a binary classification task, which requires a labeled dataset for supervised learning model training. However, the dataset generated by traditional sampling methods such as Monte Carlo sampling (MCS) and LHS is usually unbalanced. Moreover, the generated samples are often far away from SSRB, failing to accurately reflect the real characteristics of SSRB. To address these issues, this part proposes a boundary sample search algorithm. For each sample x_i within the initial sample set sample sample sample sample <math>sample sample sample

$$\left\| \boldsymbol{x}_{u,i} - \boldsymbol{x}_{s,i} \right\|^2 \le \xi \tag{14}$$

where $\|\cdot\|^2$ denotes the two-norm of vectors; and ξ is the boundary distance threshold, which represents the maximum Euclidean distance of boundary sample pairs. This threshold can be set according to engineering requirements, as shown in Fig. 3, where P_1 and P_2 represent a two-dimensional power injection space. Finally, the boundary samples set \mathbb{S}_B is generated by Algorithm 1.

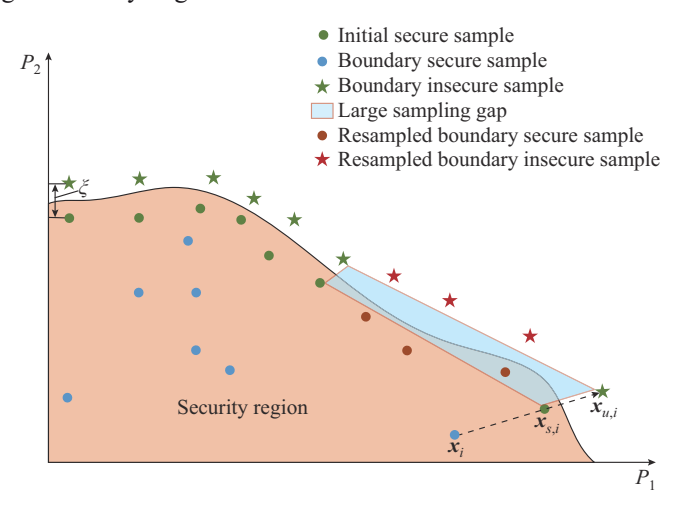


Fig. 3. Boundary sample search and resampling mechanism.

Algorithm 1: boundary sample search

```
Input: \mathbb{S}, \xi, and initial step size \lambda_{r,set}
1: Sample N<sub>S</sub> power growth direction vectors based on LHS. Each direc-
          tion vector is normalized to form the direction vector matrix
          U \in \mathbb{R}^{N_s \times N_s}
2: for x_i in \mathbb{S} do
        \lambda_r = \lambda_{r,set}
3:
         while x_i in the security region do
5:
              \mathbf{x}_i = \mathbf{x}_i + \lambda_r \mathbf{U}_i
6:
         end while
         \mathbf{x}_{s.i} = \mathbf{x}_{s.i} - \lambda_r \mathbf{U}_i, \ \mathbf{x}_{y.i} = \mathbf{x}_i
7:
8:
         while ||x_{u,i} - x_{s,i}||^2 > \xi do
              \lambda_r = 1/2\lambda_r
10:
              \boldsymbol{x}_{u,i} = \boldsymbol{x}_i - \lambda_r \boldsymbol{U}_i
11:
              if x_{u,i} is not in the security region then
12:
                  \boldsymbol{x}_{s,i} = \boldsymbol{x}_{s,i}, \ \boldsymbol{x}_{u,i} = \boldsymbol{x}_{u,i}
13:
14:
                  \mathbf{x}_{s,i} = \mathbf{x}_{s,i} + \lambda_r \mathbf{U}_i, \ \mathbf{x}_{u,i} = \mathbf{x}_{u,i} + \lambda_r \mathbf{U}_i
15:
              end if
16: end while
17: Store (x_{s,i}, 0), (x_{u,i}, 1) in \mathbb{S}_B
18: end for
Output: S,
```

As mentioned in Section II, SSR is uniquely determined, connected, and internally void-free under a given network topology and system component parameters. Therefore, when starting from a secure sample and slowly increasing the injected power in a quasi-steady state, the SSRB must be encountered. Thus, the convergence of the Algorithm 1 is guaranteed when the λ_r is set appropriately.

3) Resampling Mechanism Considering Sampling Gaps

After the boundary sample set is formed, certain security region boundaries may still have large sampling gaps, which leads to the situation that subsequent models inaccurately estimate the boundaries of these regions [34], as shown in Fig. 2. To this end, this paper proposes a resampling mechanism that considers the sampling gap based on the boundary sample set. Specifically, all the secure samples in the boundary sample set are extracted to form a matrix $X_s = \begin{bmatrix} x_{s,1}, x_{s,2}, ..., x_{s,N_s} \end{bmatrix}^T \in \mathbb{R}^{N_s \times N_p}$. The distance matrix D_{dist} is then constructed by calculating the pairwise Euclidean distances between N_s samples.

As shown in Fig. 3, for the sample $x_{s,i}$, we set the minimum value of the distance from the other samples as $D_{\min,i} = \min(D_{dist,i,:}) = D_{dist,i,j}$. We set the maximum sampling gap as Δ . When $D_{\min,i} > \Delta$, it is necessary to resample N_r samples between the sample $x_{s,i}$ and $x_{s,j}$. Then, we search for the boundary sample pair according to Algorithm 1 and add them to S_B . Typically, we perform resampling for N_{re} rounds.

B. Feature Non-linear Conversion and Boundary Linear Approximation

Due to the high-dimensionality, non-convexity, and non-linearity of the SSRB, the boundary dataset generated above is non-linearly separable. This poses a challenge to accurately approximate the boundary using linear classification methods such as DTs. Therefore, this paper proposes a method to convert the boundary samples from the original active power injection space to a 3-dimensional feature space. This is achieved by designing a non-linear feature converter, which renders the sample set linearly separable and simultaneously facilitates visualization. Ultimately, the security region boundary is linearly fitted in the feature space, and the boundary conservative translation is performed to enhance its security. This translation is crucial in achieving a more accurate and reliable SSRB.

1) Feature Non-linear Conversion Using DNNs

DNNs possess an exceptional ability for non-linear approximation. Through multi-layer non-linear transformations, DNNs progressively model the original data and map it onto a space that is nearly linearly separable. In this subsection, we convert the original power injection space into a 3-dimensional feature space using different types of DNNs. Depending on the dataset, diverse DNNs can be chosen to achieve optimal results.

In this subsection, we introduce two types of feature nonlinear converters. ① Type 1: a converter based on fully connected neural networks (FCNs). FCN is a simple type of neural network that can serve as a feature non-linear converter when dealing with low-dimensional features and a small number of samples. ② Type 2: a converter based on 1-dimensional CNN (1D-CNN). CNN incorporates convolutional processing of features into DNNs and is more suitable for processing higher dimensional data. For the datasets with higher feature dimensions and larger volumes of data, more complex neural networks such as transformers [35] can also be used as feature non-linear converters.

As an illustration, we will use the type 2 converter to demonstrate the conversion of the power injection space $\mathbb{X} \in \mathbb{R}^{N_p}$ into the feature space $\mathbb{Z} \in \mathbb{R}^3$. The feature non-linear converter based on 1D-CNN is depicted in Fig. 4.

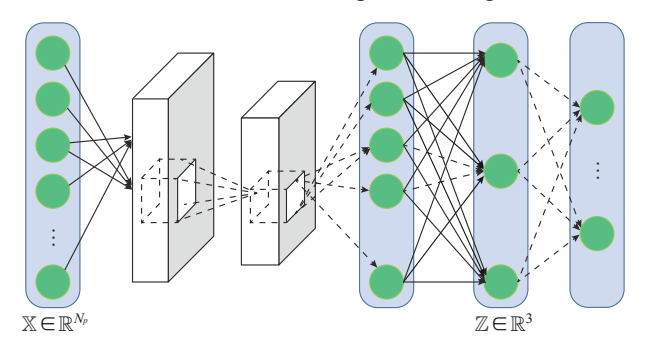


Fig. 4. Feature non-linear converter based on 1D-CNN.

2) Boundary Linear Approximation Using IGR-WODT

As mentioned above, DNNs are used as a feature non-linear converter to enhance the linear separability of the dataset. In this part, the boundary linear approximation using IGR-WODT in the feature space is performed.

IGR-WODT is improved by WODT [36], [37]. The objective function of WODT is based on weighted information entropy, which can be influenced by the number of samples and may not be optimal for model training. Therefore, IGR-WODT uses the information gain rate as its objective function instead. For a labeled binary classification dataset $S_z = \{(z_1, y_1), (z_2, y_2), ..., (z_{2N_s}, y_{2N_s})\}$, IGR-WODT first divides the training set S_z into two subsets based on a logistic regression model, and recursively generates child nodes based on the divided subsets until the terminal condition is satisfied. Specifically, at each node, IGR-WODT calculates the probability that the i^{th} sample belongs to the left subset p_i^L versus the right subset p_i^R , which is expressed as:

$$\begin{cases} p_i^L = \sigma\left(-\boldsymbol{\theta}^{\mathrm{T}} \boldsymbol{z}_i\right) = \frac{1}{1 + \mathrm{e}^{\boldsymbol{\theta}^{\mathrm{T}} \boldsymbol{z}_i}} \\ p_i^R = 1 - \sigma\left(-\boldsymbol{\theta}^{\mathrm{T}} \boldsymbol{z}_i\right) = \frac{1}{1 + \mathrm{e}^{-\boldsymbol{\theta}^{\mathrm{T}} \boldsymbol{z}_i}} \end{cases}$$
(15)

where z_i is the i^{th} sample of \mathbb{S}_z ; $\sigma(\cdot)$ is the sigmoid function; $\theta \in \mathbb{R}^{4 \times 1}$ is the vector of model parameters (including a bias), which needs to be continuously updated during the model training process. When $p_i^L \ge 0.5$, the i^{th} sample is classified as belonging to the left subset; when $p_i^R > 0.5$, the i^{th} sample is classified as belonging to the right subset.

The weights of each sample set are defined as:

$$\begin{cases} w_i^L = p_i^L \\ w_i^R = p_i^R \end{cases} \tag{16}$$

Therefore, IGR-WODT defines 2 datasets associated with sample weights as:

$$\begin{cases}
\mathbb{S}_{L} = \left\{ \left(z_{i}, y_{i}, w_{i}^{L} \right) \middle| \left(z_{i}, y_{i} \right) \in \mathbb{S}_{z} \right\} \\
\mathbb{S}_{R} = \left\{ \left(z_{i}, y_{i}, w_{i}^{R} \right) \middle| \left(z_{i}, y_{i} \right) \in \mathbb{S}_{z} \right\}
\end{cases}$$
(17)

IGR-WODT calculates the empirical entropy $H(\mathbb{S}_z)$ of the dataset \mathbb{S}_z , and the conditional empirical entropy $H(\mathbb{S}_z|\boldsymbol{\theta})$ of the dataset \mathbb{S}_z under the division of $\boldsymbol{\theta}^T z$.

$$H(S_z) = -\sum_{k=1}^{K} \frac{|S_k|}{|S_z|} \log_2 \frac{|S_k|}{|S_z|}$$

$$H(S_z|\theta) = \frac{|S_L|}{|S_z|} H(S_L) + \frac{|S_R|}{|S_z|} H(S_R)$$
(18)

where $|S_z|$ is the number of samples in the dataset S_z , which is equal to $2N_s$; and $|S_k|$ is the number of samples in the dataset $|S_z|$ with the category k:

$$\begin{cases}
\left| \mathbb{S}_{L} \right| = \sum_{(x_{i}, y_{i}, w_{i}^{L}) \in \mathbb{S}_{L}} w_{i}^{L} \\
\left| \mathbb{S}_{R} \right| = \sum_{(x_{i}, y_{i}, w_{i}^{R}) \in \mathbb{S}_{R}} w_{i}^{R} \\
H\left(\mathbb{S}_{L}\right) = -\sum_{k=1}^{K} \frac{W_{L}^{k}}{\left| \mathbb{S}_{L} \right|} \log_{2} \frac{W_{L}^{k}}{\left| \mathbb{S}_{L} \right|} \\
H\left(\mathbb{S}_{R}\right) = -\sum_{k=1}^{K} \frac{W_{R}^{k}}{\left| \mathbb{S}_{R} \right|} \log_{2} \frac{W_{R}^{k}}{\left| \mathbb{S}_{R} \right|}
\end{cases}$$
(19)

$$\begin{cases} W_L^k = \sum_{(x_i, y_i, w_i^L) \in S_L} I(y_i = k) w_i^L \\ W_R^k = \sum_{(x_i, y_i, w_i^R) \in S_R} I(y_i = k) w_i^R \end{cases}$$
(20)

where $I(\cdot)$ is the indicator function; W_L^k represents the sum of w_i^L corresponding to the samples of category k in set \mathbb{S}_L ; and W_R^k represents the sum of w_i^R corresponding to the samples of category k in set \mathbb{S}_R .

As shown in (18) and (19), $H(\mathbb{S}_z)$, $H(\mathbb{S}_z|\theta)$, $H(\mathbb{S}_L)$, and $H(\mathbb{S}_R)$ are all calculated based on the probabilities of the i^{th} sample belonging to the left or right child node.

IGR-WODT defines the information gain rate as:

$$g_{R}(\boldsymbol{\theta}) = \frac{H(\mathbb{S}_{z}|\boldsymbol{\theta})}{H(\mathbb{S}_{z})}$$
 (21)

To avoid overfitting of the model under each node, the regularization term L_2 is introduced and the final model objective function expressed as:

$$L(\boldsymbol{\theta}) = \frac{H(S_{z}|\boldsymbol{\theta})}{H(S_{z})} + \eta \|\boldsymbol{\theta}\|^{2}$$
(22)

where η is the coefficient of the regularization term L_2 .

To optimize the objective function $L(\theta)$, IGR-WODT employs the improved Broyden-Fletcher-Goldfarb-Shanno (BFGS) algorithm [37] to obtain the optimal parameters $\theta_{hest} = \arg\min L(\theta)$. Thus, the dataset S_z is divided into left

and right subsets \mathbb{S}'_L and \mathbb{S}'_R using the parameters $\boldsymbol{\theta}_{best}$. The details of IGR-WODT algorithm are shown in Algorithm SA1 in Supplementary Material A.

Then, we extract the decision parameters, i. e., θ , from IGR-WODT to construct the SSRB hyperplane in the feature space. Algorithm SA2 in Supplementary Material A provides a detailed depiction. The essence of the Algorithm SA2 lies in identifying all decision paths within IGR-WODT that lead from the root node to the leaf node labeled as 0. These paths are then transformed into a combination of hyperplanes by converting θ of all the nodes along these paths.

IV. CASE STUDY

This section validates the effectiveness and generality of the proposed high-dimensional SSRB approximation model on the WECC 3-machine 9-bus system and IEEE 118-bus system using PYPOWER [38]. The system component parameters and steady-state security constraints, such as the upper and lower limits of generator output, are referenced from [38]. The upper voltage limit is set to be 1.05, and the lower voltage limit is set to be 0.95. All experiments are implemented on a Linux workstation equipped with an Intel^(R) Xeon^(R) Gold 6132 2.60 GHz CPU processor.

A. Case 1: WECC 3-machine 9-bus System

As shown in Fig. 5, the WECC 3-machine 9-bus system contains 3 generators (G1-G3) and 3 load nodes. Bus 1 is set as the slacking bus. The active power injection space in WECC 3-machine 9-bus system is $\left[P_{g,2}, P_{g,3}, P_{l,5}, P_{l,7}, P_{l,9}\right]$.

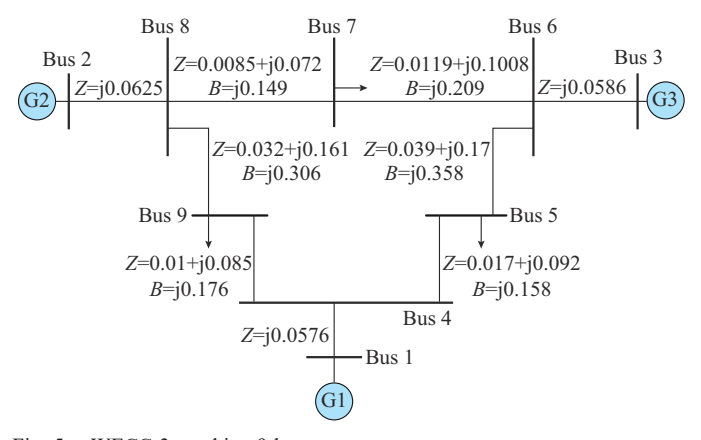


Fig. 5. WECC 3-machine 9-bus system.

1) 2-dimensional Active Power Injection SSRB Analysis

To demonstrate the non-convexity and non-linearity of SS-RB in power systems intuitively, we first study the SSRB in the power injection space $[P_{l,5}, P_{l,9}]$, i.e., we set $[P_{g,2}, P_{g,3}, P_{l,7}]$ as constant values.

The boundary samples are searched according to the method proposed in Section III and shown in Fig. 6. Figure 6(f) depicts the whole SSR, which is the intersection of the static voltage security region, the generator output security region, and the branch thermal stability security region. This region is closed, with non-convex and non-linear boundaries, making it challenging to directly separate the boundary dataset.

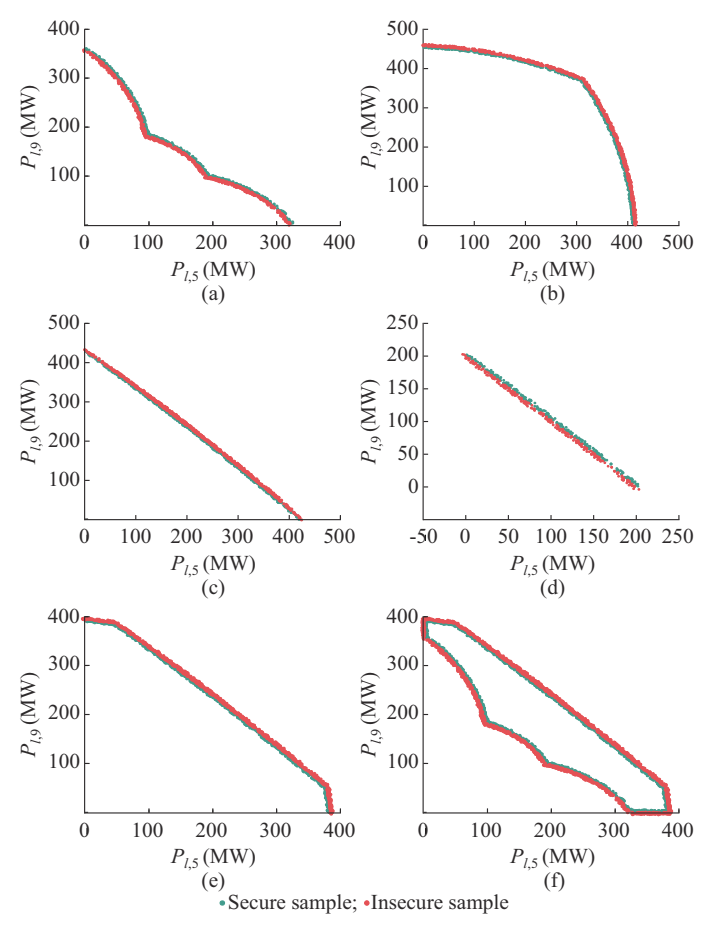


Fig. 6. 2-dimensional SSRB samples on WECC 3-machine 9-bus system. (a) Upper boundary samples of node voltages. (b) Lower boundary samples of node voltages. (c) Upper boundary samples of generator outputs. (d) Lower boundary samples of generator outputs. (e) Boundary samples of branch thermal security. (f) Whole SSR.

We further analyze the impact of different setting values of upper and lower voltage limits on the characteristics of the SSRB. When the voltage range is set between 0.98 p.u. and 1.02 p.u., the 2-dimensional SSRB samples is presented, as shown in Fig. 7.

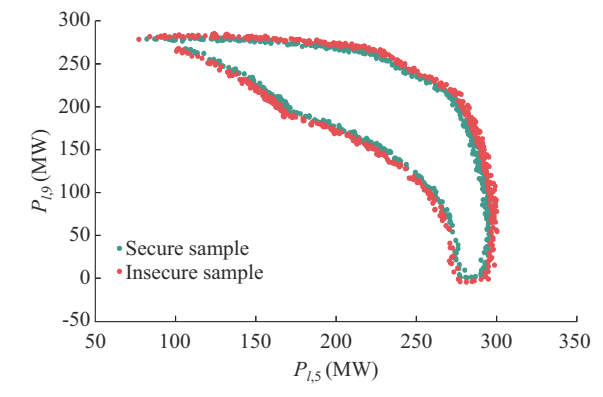


Fig. 7. 2-dimensional SSRB samples when voltage range is set between $0.98~\mathrm{p.u.}$ and $1.02~\mathrm{p.u.}$.

Compared with Fig. 6(f), the boundary shape has changed significantly, with the non-convex and non-linear characteristics further highlighted. This is because the non-linear map-

ping relationship between the static voltage security region and the power injection space is more complex than that of the security region of branch thermal stability and the generator output security region. Therefore, the stricter the system requirement for the voltage range is, the more complex the SSRB characteristics will be.

Therefore, even if the boundary is approximated by segmented linear approximation, the error can still be significant, especially in high-dimensional spaces. To address this issue, the original power injection space needs to be converted into a new feature space using the feature non-linear converter, and then the linear approximation of the boundary can be performed.

2) SSRB Approximation for WECC 3-machine 9-bus System Under Active Power Injection

For the WECC 3-machine 9-bus system, SSRB under active power injection is 5-dimensional. The power injection space is $[P_{g,2}, P_{g,3}, P_{L5}, P_{L7}, P_{L9}]$.

We first generate the initial samples using the proposed sampling method. To validate the efficiency of the proposed sampling method, we compare it with the LHS, MCS, importance sampling (IS), and Markov chain Monte Carlo sampling (MCMCS). The proportion of secure samples in the initially generated samples is used as the benchmark for the evaluation. The experiments are performed with five different random seeds, and the results are presented in Table I.

TABLE I
COMPARISON OF DIFFERENT SAMPLING METHODS IN WECC 3-MACHINE
9-BUS SYSTEM

Method	Number of secure samples	Proportion of secure samples (%)
Proposed	17402 ± 61	87.01 ± 0.31
LHS	1885 ± 66	9.43 ± 0.33
MCS	1873 ± 26	9.37 ± 0.13
IS	1986 ± 46	9.93 ± 0.23
MCMCS	1894 ± 53	9.47 ± 0.26

Table I demonstrates that the proposed sampling method yields a considerably higher proportion of secure samples in the sampled dataset compared with traditional LHS, MCS, IS, and MCMCS methods. After generating the initial dataset, Algorithm 1 is used to search for boundary samples. A total of 17437 pairs of samples are obtained. After 10 rounds of resampling, additional 5241 sample pairs are added to form the final boundary sample set.

Since the dimension of the SSRB under active power injection space for the WECC 3-machine 9-bus system is 5, an FCN with three hidden layers (64, 16, 3 neurons) and one output layer is chosen as the feature non-linear converter. The Adam optimization algorithm is selected for training. The boundary sample pairs are split into training and validation sets according to 8:2.

After 1000 rounds of training, the optimal model is selected, and feature conversion is performed. Figure 8 shows SS-RB and sample distribution in 3-dimensional feature space.

With the dataset in the feature space, the original dataset can be divided accurately by a finite number of hyperplanes.

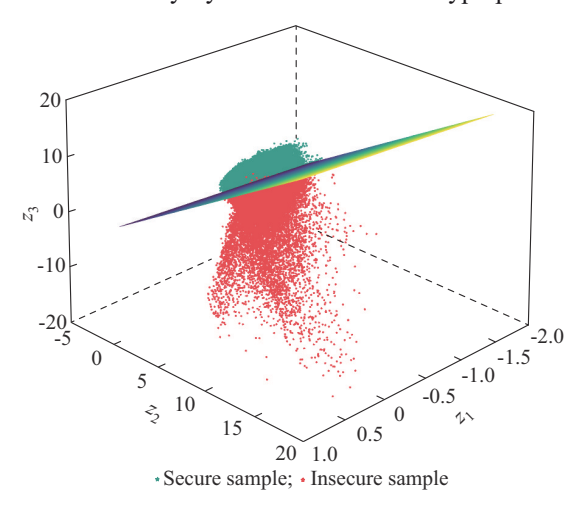


Fig. 8. SSRB and sample distribution in 3-dimensional feature space.

Therefore, the training and validation sets are converted into the feature space by the trained FCN model respectively, and the boundaries are fitted using IGR-WODT. The maximum depth of IGR-WODT is set between 1 and 4, and the L_2 regularization coefficient η is set to be 10^{-5} .

To test the validity of the boundary in a more general way, 20000 samples (not boundary samples) are generated as the test set based on the proposed sampling method. The accuracy P_{acc} , precision P_{pre} , and recall rate P_{rec} are also introduced to evaluate the model performance, which are calculated as (23).

$$P_{acc} = \frac{T_P + T_N}{T_P + T_N + F_N + F_P}$$

$$P_{pre} = \frac{T_P}{T_P + F_P}$$

$$P_{rec} = \frac{T_P}{T_P + F_N}$$
(23)

where T_P is the number of samples labeled as secure and judged as secure; T_N is the number of samples labeled as insecure and judged as insecure; $F_{\scriptscriptstyle N}$ is the number of samples labeled as secure and judged as insecure; F_P is the number of samples labeled as insecure and judged as secure; P_{acc} is the proportion of correctly classified samples in the dataset and reflects the overall performance of the proposed sampling method; P_{pre} is the proportion of samples that are truly secure among those classified as secure by the model, reflecting the security of the fitted boundary; and P_{rec} is the proportion of secure samples that are correctly classified in the dataset, reflecting the conservativeness of the boundary to some extent. In this paper, it is crucial to minimize the number of insecure samples classified as secure samples, i.e., minimize F_n , thus a conservative translation of the fitted boundary is required.

Table II presents the model performance on WECC 3-machine 9-bus system, presenting the performance of each model on the training, validation, and test sets. In Table II, UDT represents univariate DT. UDT without FNC and IGR-

WODT without FNC represent that DT models split the original dataset directly without using feature non-linear convert-

TABLE II							
MODEL PERFORMANCE ON WECC 3-MACHINE 9-BUS SYSTEM							

Model	Depth	Training set		Validation set			Test set			
		P_{acc}	P_{pre}	P_{rec}	P_{acc}	P_{pre}	P_{rec}	P_{acc}	P_{pre}	P_{rec}
UDT	1	0.9907	0.9876	0.9938	0.9881	0.9843	0.9921	0.9957	0.9967	0.9983
	2	0.9924	0.9869	0.9982	0.9898	0.9830	0.9967	0.9959	0.9966	0.9987
	3	0.9943	0.9933	0.9953	0.9929	0.9923	0.9936	0.9959	0.9981	0.9972
	4	0.9946	0.9947	0.9945	0.9922	0.9929	0.9914	0.9956	0.9986	0.9963
UDT without FNC	1	0.5637	0.5340	1.0000	0.5648	0.5347	0.9998	0.8717	0.8719	0.9998
	2	0.6049	0.5586	1.0000	0.6058	0.5592	1.0000	0.8715	0.8719	0.9994
	3	0.6412	0.5822	1.0000	0.6438	0.5840	1.0000	0.8715	0.8718	0.9991
	4	0.6412	0.5822	1.0000	0.6438	0.5840	1.0000	0.8712	0.8718	0.9991
IGR-WODT	1	0.9944	0.9936	0.9953	0.9929	0.9927	0.9932	0.9957	0.9985	0.9965
	2	0.9944	0.9937	0.9951	0.9931	0.9927	0.9934	0.9957	0.9985	0.9965
	3	0.9944	0.9924	0.9964	0.9923	0.9938	0.9938	0.9957	0.9985	0.9965
	4	0.9946	0.9943	0.9949	0.9926	0.9923	0.9929	0.9957	0.9985	0.9965
IGR-WODT without FNC	1	0.5637	0.5340	1.0000	0.5648	0.5347	1.0000	0.8717	0.8719	0.9998
	2	0.6049	0.5586	1.0000	0.6058	0.5592	1.0000	0.8715	0.8719	0.9994
	3	0.6411	0.5821	1.0000	0.6438	0.5840	1.0000	0.8713	0.8718	0.9992
	4	0.6638	0.5980	1.0000	0.6642	0.5983	1.0000	0.8713	0.8718	0.9992
Translated boundary		0.9563	0.9998	0.9129	0.9559	0.9993	0.9124	0.9865	0.9999	0.9846

As shown in Table II, DT models using feature non-linear converters exhibit significant improvements in performance compared with DT models that do not use feature non-linear converters. The former achieves an accuracy of about 99% for the validation set, while the latter only achieves about 66%. The former also shows an accuracy improvement of about 12% for the test set. These results confirm the superiority of the proposed sampling method in solving non-convex and non-linear SSRB. Moreover, when using feature non-linearity converters, the proposed IGR-WODT outperforms UDT.

IGR-WODT achieves high accuracy across all indicators at the depth of 1, with an accuracy exceeding 99.29% in the training, validation, and test sets. Therefore, IGR-WODT with the depth of 1 is selected as the boundary approximation model, and its security region boundary under the feature space is shown in (24), which is constructed using Algorithm SAII of Supplementary Material A.

$$-0.5654z_1 - 9.0060z_2 + 8.7684z_3 > 0.1745 \tag{24}$$

To enhance the ability of the model to distinguish insecure samples more accurately, the boundary is conservatively translated. This means that the insecured samples, currently designated as security by the existing boundary, are reclassified as outside the security region.

Specifically, the distance between insecure samples within the current security region of the training set and the current SSRB is calculated. There are 117 insecure samples within this region, and their distances from the current boundary are presented, as shown in Fig. 9. and the depth color represents the magnitude of corresponding values.

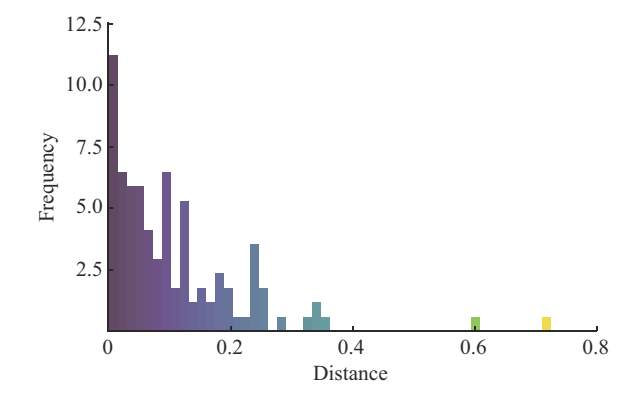


Fig. 9. Distance distribution of insecure samples within security region from boundary for WESS 3-machine 9-bus system.

As shown in Fig. 9, 99% of the insecure samples within the security region are distributed within the distance of 0.35 from the current SSRB. Therefore, the SSRB is translated by 0.35 towards the non-security region. The new SSRB is shown in (25) and visualized in Fig. 8. It is evident that the plane effectively distinguishes the secure samples from the insecure ones.

$$-0.5654z_1 - 9.0060z_2 + 8.7684z_3 > 4.5775$$
 (25)

The performance on datasets under the new boundary is shown in Table II. After applying the aforementioned boundary conservative translation, it is evident that the precision on the test set has improved significantly, reaching above 99.99%, which indicates an increase in the reliability of the fitted boundary. Furthermore, the accuracy and recall rate on the test set also reach 98.65% and 99.26%, respectively, verifying the rationality and effectiveness of the proposed sam-

pling method.

To further evaluate the computational efficiency of the proposed sampling method, we compare it with the pointwise method by calculating the time required for each method to classify the state of 20000 samples in the test set. The results shown in Table III indicate that the proposed sampling method is nearly 2600 times faster than the pointwise method, taking only 0.2 s to classify 20000 samples, which meets the requirements for online applications.

TABLE III

COMPARISON OF COMPUTATIONAL EFFICIENCY OF DIFFERENT SAMPLING
METHODS ON WECC 3-MACHINE 9-BUS SYSTEM

Method	Time (s)			
Proposed sampling method	0.20			
Pointwise method	524.77			

B. Case 2: IEEE 118-bus System

In order to further verify the effectiveness and generality of the proposed sampling method in the high-dimensional SSRB approximation of large-scale power systems, the proposed sampling method is verified on the IEEE 118-bus system. The IEEE 118-bus system is configured with 54 generators and 99 load nodes, with bus 69 set as the slacking bus, whose active power injection space is 152-dimensional.

Similar to the experiments on the WECC 3-machine 9-bus system, the proposed sampling method is compared with the LHS, MCS, IS, and MCMCS methods. The experiments are

performed with five different random seeds. The results are investigated, as shown in Table IV, where the proportion of secure samples generated by the proposed sampling method is significantly increased.

Method	Number of secure samples	Proportion of secure samples (%)		
Proposed sampling method	87293 ± 127	87.29 ± 0.13		
LHS	22990 ± 241	22.99 ± 0.24		
MCS	23025 ± 120	23.03 ± 0.12		
IS	23145 ± 167	23.14 ± 0.17		
MCMCS	22885 ± 124	22.89 ± 0.12		

After completing the search for boundary samples, 87268 pairs of boundary sample pairs are obtained. A 1D-CNN based feature non-linear converter is designed for the IEEE 118-bus system, containing one layer of 1D-CNN and three layers of FCN with the number of neurons being 128, 64, and 3, respectively. The aforementioned boundary sample pairs are divided into training and validation sets according to 8:2. Additionally, 100000 samples, which are not boundary samples, are generated as the test set.

After 1000 rounds of training, we select the optimal model as the feature non-linear converter. The performance of the SSRB fitted using IGR-WODT in the feature space is presented in Table V.

TABLE V MODEL PERFORMANCE ON IEEE 118-BUS SYSTEM

Model	Depth	Training set		Validation set			Test set			
		P_{acc}	P_{pre}	P_{rec}	P_{acc}	P_{pre}	P_{rec}	P_{acc}	P_{pre}	P_{rec}
UDT	1	0.9673	0.9705	0.9639	0.9429	0.9438	0.9418	0.9483	0.9770	0.9634
	2	0.9747	0.9776	0.9615	0.9469	0.9504	0.9323	0.9483	0.9770	0.9634
	3	0.9791	0.9766	0.9819	0.9497	0.9492	0.9503	0.9481	0.9759	0.9643
	4	0.9803	0.9717	0.9894	0.9502	0.9426	0.9589	0.9503	0.9702	0.9729
	1	0.9807	0.9800	0.9815	0.9511	0.9491	0.9533	0.9490	0.9731	0.9683
ICD WODT	2	0.9800	0.9755	0.9847	0.9512	0.945	0.9581	0.9495	0.9724	0.9696
IGR-WODT	3	0.9805	0.9820	0.9792	0.9507	0.9511	0.9503	0.9485	0.9740	0.9667
	4	0.9807	0.9803	0.9812	0.9504	0.9507	0.9500	0.9483	0.9742	0.9664
Franslated boundary		0.9385	0.9991	0.8771	0.9205	0.9846	0.8543	0.9223	0.9882	0.9219

As shown in Tables II and V, both IGR-WODT and UDT demonstrate outstanding performance in the feature space. Additionally, in terms of $P_{\it acc}$, the performance is comparable to the IGR-WODT with depth of 1 only when the UDT depth is 4. This trend becomes more evident in large-scale power systems, as presented in Table V. Thus, IGR-WODT achieves a balance between high accuracy and low model complexity.

Given the comparable performance, the model with lower complexity is chosen as the boundary approximation model, which is the IGR-WODT model with the depth of 1. Its boundary expression is shown in (26).

$$-0.0932z_1 - 5.8812z_2 + 7.0016z_3 > -0.7624$$
 (26)

Similar to Case 1, a conservative translation of the aforementioned boundary is performed. One thousand three hundred and ninety nine insecure samples are located within the current security region. The distances between these samples and the current SSRB are distributed. As shown in Fig. 10, the distance of the insecure samples in the current security region from the SSRB is 95% distributed within 1.0. Thus, the security region boundary is translated towards the non-security region by 1.0. Here, the distance of the boundary translation can be selected according to the requirements in practical engineering applications. The new security region boundary is given by:

$$-0.0932z_1 - 5.8812z_2 + 7.0016z_3 > 8.3819 \tag{27}$$

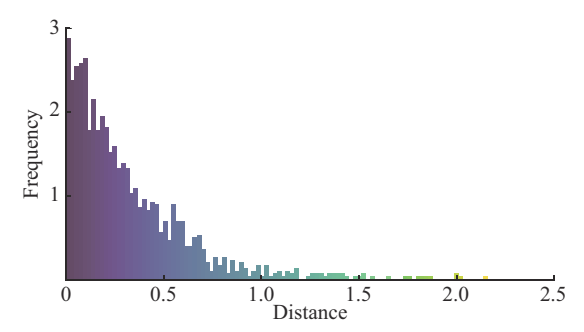


Fig. 10. Distance distribution of insecure samples within security region from boundary for IEEE 118-bus system.

Table V displays the performance of each model on the training, validation, and test sets. The results show that the fitted boundary achieves an accuracy and a recall rate of 92.23% and 92.19%, respectively, while maintaining a precision of 98.82% on the test set. The results in Table V indicate that the proposed sampling method achieves similar performance in solving high-dimensional SSRB with 152 dimensions as in Case 1. This can be attributed to the incorporation of a CNN layer into the feature non-linear converter designed for Case 2, which can better capture high-dimensional feature information. These results confirm the effectiveness and versatility of the proposed sampling method in modeling high-dimensional SSRB.

We conduct a further comparison of the computational efficiency between the proposed sampling method and the pointwise method in Case 2. Specifically, we analyze the time required to assess the states of 100000 operating points for both methods. As illustrated in Table VI, the proposed sampling method demonstrates several hundred times improvement in computational efficiency compared with the pointwise method, requiring only approximately 10 s. This demonstrates that the proposed sampling method satisfactorily meets the demands for online applications in large-scale power systems.

TABLE VI

COMPARISON OF COMPUTATIONAL EFFICIENCY OF DIFFERENT SAMPLING
METHODS IN IEEE 118-BUS SYSTEM

Method	Time (s)
Proposed sampling method	10.32
Pointwise method	2677.71

Further, considering the noise interference and data missing during data measurement and transmission process in real power systems, we conduct experiments to test the proposed sampling method. Specifically, we add Gaussian random noise with a range from -1 to 1 to a randomly selected 10% of the dataset and simultaneously nullified 0.1% of the data to simulate the aforementioned issues. The performance of the proposed sampling method on the dataset is subjected to noise interference and data missing, as shown in Fig. 11.

As shown in Fig. 11, while maintaining P_{pre} essentially unchanged, the decline in P_{acc} and P_{rec} is less than 5%, which indicates that the proposed sampling method exhibits good robustness on datasets subjected to noise interference and da-



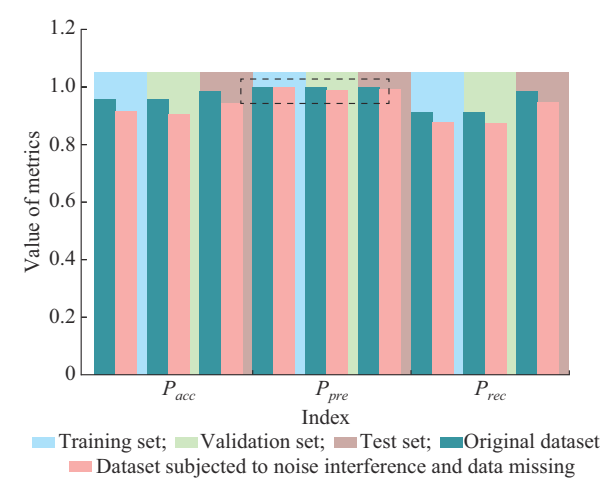


Fig. 11. Model performance on dataset subjected to noise interference and data missing.

V. CONCLUSION AND FUTURE WORK

This paper proposes a novel method to approximate the high-dimensional SSRB via the feature non-linear converter and improved oblique DT. The proposed sampling method is evaluated on the WECC 3-machine 9-bus system and IEEE 118-bus system. The experimental results demonstrate that it outperforms previous methods by effectively approximating the high-dimensional boundary and reducing the error between the approximated and real boundaries. As shown in Tabels II and V, the accuracy and recall rate are both above 92% while the precision achieves 98% for the tested systems. Also, the proposed sampling method exhibits good robustness on datasets subjected to noise interference and data missing, as can be observed in Fig. 11.

Future research work will mainly focus on: ① integrating renewable energy and load forecasting tools to assess the system state in real-time within N time steps based on the proposed sampling method, and guiding the formulation of real-time dispatch and control strategies for power systems; and ② data-driven methods for predicting the steady-state security margin.

REFERENCES

- [1] A. Moreira, D. Pozo, A. Street *et al.*, "Reliable renewable generation and transmission expansion planning: co-optimizing system's resources for meeting renewable targets," *IEEE Transactions on Power Systems*, vol. 32, no. 4, pp. 3246-3257, Jul. 2017.
- [2] J. Xu, H. Gao, R. Wang et al., "Real-time operation optimization in active distribution networks based on multi-agent deep reinforcement learning," *Journal of Modern Power Systems and Clean Energy*, vol. 12, no. 3, pp. 886-899, May 2020.
- [3] S. Li, D. Cao, W. Hu et al., "Multi-energy management of interconnected multi-microgrid system using multi-agent deep reinforcement learning," *Journal of Modern Power Systems and Clean Energy*, vol. 11, no. 5, pp. 1606-1617, Sept. 2023.
- [4] Y. Yu, Y. Liu, C. Qin et al., "Theory and method of power system integrated security region irrelevant to operation states: an introduction," Engineering, vol. 6, no. 7, pp. 754-777, Jul. 2020.
- [5] H.-D. Chiang and C.-Y. Jiang, "Feasible region of optimal power flow: characterization and applications," *IEEE Transactions on Power Systems*, vol. 33, no. 1, pp. 236-244, Jan. 2018.
- [6] J. Xiao, G. Zu, X. Gong et al., "Observation of security region boundary for smart distribution grid," IEEE Transactions on Smart Grid,

- vol. 8, no. 4, pp. 1731-1738, Jul. 2017.
- [7] S. Chen, Z. Wei, G. Sun et al., "Convex hull based robust security region for electricity-gas integrated energy systems," *IEEE Transactions on Power Systems*, vol. 34, no. 3, pp. 1740-1748, May 2019.
- [8] T. Ding, R. Bo, H. Sun et al., "A robust two-level coordinated static voltage security region for centrally integrated wind farms," IEEE Transactions on Smart Grid, vol. 7, no. 1, pp. 460-470, Jan. 2016.
- [9] S. Chen, Q. Chen, Q. Xia et al., "Steady-state security assessment method based on distance to security region boundaries," *IET Genera*tion, Transmission & Distribution, vol. 7, no. 3, pp. 288-297, Mar. 2013.
- [10] F. Wu and S. Kumagai, "Steady-state security regions of power systems," *IEEE Transactions on Circuits and Systems*, vol. 29, no. 11, pp. 703-711, Nov. 1982.
- [11] H. D. Nguyen, K. Dvijotham, and K. Turitsyn, "Constructing convex inner approximations of steady-state security regions," *IEEE Transac*tions on Power Systems, vol. 34, no. 1, pp. 257-267, Jan. 2019.
- [12] D. Lee, H. D. Nguyen, K. Dvijotham et al., "Convex restriction of power flow feasibility sets," *IEEE Transactions on Control of Network* Systems, vol. 6, no. 3, pp. 1235-1245, Sept. 2019.
- [13] X. Li, T. Jiang, L. Bai et al., "Orbiting optimization model for tracking voltage security region boundary in bulk power grids," CSEE Journal of Power and Energy Systems, vol. 8, no. 2, pp. 476-487, Mar. 2022.
- [14] T. Jiang, R. Zhang, X. Li et al., "Integrated energy system security region: concepts, methods, and implementations," Applied Energy, vol. 283, p. 116124, Feb. 2021.
- [15] X. Li, G. Tian, Q. Shi et al., "Security region of natural gas network in electricity-gas integrated energy system," *International Journal of Electrical Power & Energy Systems*, vol. 117, p. 105601, May 2020.
- [16] X. Li, T. Jiang, G. Liu et al., "Bootstrap-based confidence interval estimation for thermal security region of bulk power grid," *International Journal of Electrical Power & Energy Systems*, vol. 115, p. 105498, Feb. 2020.
- [17] T. Yang and Y. Yu, "Static voltage security region-based coordinated voltage control in smart distribution grids," *IEEE Transactions on Smart Grid*, vol. 9, no. 6, pp. 5494-5502, Nov. 2018.
- [18] R. Yan, G. Geng, and Q. Jiang, "Data-driven transient stability boundary generation for online security monitoring," *IEEE Transactions on Power Systems*, vol. 36, no. 4, pp. 3042-3052, Jul. 2020.
- [19] J. An, J. Yu, Z. Li et al., "A data-driven method for transient stability margin prediction based on security region," *Journal of Modern Power Systems and Clean Energy*, vol. 8, no. 6, pp. 1060-1069, Nov. 2020.
- [20] P. Yong, Y. Wang, T. Capuder et al., "Steady-state security region of energy hub: modeling, calculation, and applications," *International Journal of Electrical Power & Energy Systems*, vol. 125, p. 106551, Feb. 2021.
- [21] O. F. Avila, J. A. P. Filho, and W. Peres, "Steady-state security assessment in distribution systems with high penetration of distributed energy resources," *Electric Power Systems Research*, vol. 201, p. 107500, Dec. 2021.
- [22] Y. LeCun, Y. Bengio, and G. Hinton, "Deep learning," *Nature*, vol. 521, no. 7553, pp. 436-444, May 2015.
- [23] S. Wu, L. Zheng, W. Hu et al., "Improved deep belief network and model interpretation method for power system transient stability assessment," *Journal of Modern Power Systems and Clean Energy*, vol. 8, no. 1, pp. 27-37, Jan. 2020.
- [24] Z. Shi, W. Yao, L. Zeng et al., "Convolutional neural network-based power system transient stability assessment and instability mode prediction," Applied Energy, vol. 263, p. 114586, Apr. 2020.
- [25] X. Liu, X. Miao, H. Jiang et al., "Box-point detector: a diagnosis method for insulator faults in power lines using aerial images and convolutional neural networks," *IEEE Transactions on Power Delivery*, vol. 36, no. 6, pp. 3765-3773, Dec. 2021.
- [26] D. Yang, Y. Pang, B. Zhou et al., "Fault diagnosis for energy internet using correlation processing-based convolutional neural networks," IEEE Transactions on Systems, Man, and Cybernetics: Systems, vol. 49, no. 8, pp. 1739-1748, Aug. 2019.
- [27] J. van Gompel, D. Spina, and C. Develder, "Satellite based fault diagnosis of photovoltaic systems using recurrent neural networks," *Applied Energy*, vol. 305, p. 117874, Jan. 2022.
- [28] Y. Zhao, P. Liu, Z. Wang et al., "Fault and defect diagnosis of battery for electric vehicles based on big data analysis methods," Applied Energy, vol. 207, pp. 354-362, Dec. 2017.
- [29] H. Shi, M. Xu, and R. Li, "Deep learning for household load forecasting a novel pooling deep RNN," *IEEE Transactions on Smart Grid*, vol. 9, no. 5, pp. 5271-5280, Sept. 2018.

- [30] C. Hu, J. Zhang, H. Yuan et al., "Black swan event small-sample transfer learning (BEST-L) and its case study on electrical power prediction in covid-19," Applied Energy, vol. 309, p. 118458, Mar. 2022.
- [31] Y. Jiang, T. Gao, Y. Dai et al., "Very short-term residential load fore-casting based on deep-autoformer," Applied Energy, vol. 328, p. 120120, Dec. 2022.
- [32] Q. Hou, N. Zhang, D. S. Kirschen et al., "Sparse oblique decision tree for power system security rules extraction and embedding," *IEEE Transactions on Power Systems*, vol. 36, no. 2, pp. 1605-1615, Mar. 2021.
- [33] T. Behdadnia, Y. Yaslan, and I. Genc, "A new method of decision tree based transient stability assessment using hybrid simulation for real-time pmu measurements," *IET Generation, Transmission & Distribution*, vol. 15, no. 4, pp. 678-693, Dec. 2020.
- [34] R. Yan, G. Geng, and Q. Jiang, "Data-driven transient stability boundary generation for online security monitoring," *IEEE Transactions on Power Systems*, vol. 36, no. 4, pp. 3042-3052, Jul. 2021.
- [35] A. Vaswani, N. Shazeer, N. Parmar et al., "Attention is all you need," Advances in Neural Information Processing Systems, Long Beach, USA, Jun. 2017, pp. 1-10.
- [36] B. Yang, S. Shen, and W. Gao, "Weighted oblique decision trees," in Proceedings of the AAAI Conference on Artificial Intelligence, Hawaii, USA, Sept. 2019, pp. 5621-5627.
- [37] Y. Dai, Q. Chen, J. Zhang et al., "Enhanced oblique decision tree enabled policy extraction for deep reinforcement learning in power system emergency control," *Electric Power Systems Research*, vol. 209, p. 107932, Aug. 2022.
- [38] R. D. Zimmerman, C. E. Murillo-Snchez, and R. J. Thomas, "Matpower: steady-state operations, planning, and analysis tools for power systems research and education," *IEEE Transactions on Power Systems*, vol. 26, no. 1, pp. 12-19, Feb. 2011.

Yuxin Dai received the B.E. degree at the School of Automation from Central South University, Changsha, China, in 2019. From 2019, he is pursuing the Ph.D. degree at the School of Electrical and Automation, Wuhan University, Wuhan, China. His main research interests include application of deep learning, deep reinforcement learning, and other artificial intelligence algorithms in power system operation and control.

Jun Zhang received the B.E. and M.E. degrees in electrical engineering from Huazhong University of Science and Technology, Wuhan, China, in 2003 and 2005, respectively, and the Ph.D. degree in electrical engineering from Arizona State University, Phoenix, USA, in 2008. From 2011, he was an Assistant Professor and then tenured Associate Professor in Electrical and Computer Engineering at the University of Denver, Denver, USA. Currently, he is a Professor at the School of Electrical Engineering and Automation, Wuhan University, Wuhan, China. His research interests include signal processing, big data, artificial intelligence, blockchain, and their applications in complex and intelligent systems.

Peidong Xu received the M.S. and Ph.D. degrees in the School of Electrical Engineering and Automation from Wuhan University, Wuhan, China, in 2018 and 2022, respectively. Following his doctoral work, he currently works as a Research Scientist at the School of Electrical Engineering and Automation, Wuhan University. His research interests include power system operation and control, electric vehicle, and human-machine hybrid augmented intelligence.

Tianlu Gao received the master's degree from the School of Electrical and Computer, University of Denver, Denver, USA, in 2019. In the meantime, he took an internship at National Renewable Energy Laboratory (NREL), Golden, USA, as a Big Data Engineer. During 2019-2022, he worked as a Project Engineer at the School of Electrical and Automation, Wuhan University, Wuhan, China. From 2022, he is pursuing the Ph. D. degree at the School of Electrical and Automation, Wuhan University. His main research interests include application of simulation, artificial intelligence, natural language processing, and blockchain in power system operation and control.

David Wenzhong Gao received the M.S. and Ph.D. degrees in electrical and computer engineering, specializing in electric power engineering, from Georgia Institute of Technology, Atlanta, USA, in 1999 and 2002, respectively. He is currently with the Department of Electrical and Computer Engineering, University of Denver, Denver, USA. His main research interests include power system operation and control.